KAPL-P-000007
(K95065)

LASER DOPPLER VELOCIMETRY (LDV) MEASUREMENT AND NAVIER-STOKES COMPUTATION OF PARELLEL JET MIXING IN A RECTANGULAR CONFINEMENT

R. F. Kunz, S. W. D'Amico, P. F. Vassallo, M. A. Zaccaria, H. Aksoy, R. M. C. So

June 1995

NOTICE

KAPL ATOMIC POWER LABORATORY SCHENECTADY, NEW YORK 12301

Operated for the U. S. Department of Energy
by KAPL, Inc. a Lockheed Martin company

DISCLAIMER

Portions of this document may be illegible in electronic image products. Images are produced from the best available original document.

LDV Measurement and Navier-Stokes Computation of Parallel Jet Mixing in a Rectangular Confinement

Robert F. Kunz, Stephen W. D'Amico, Peter F. Vassallo, Michael A. Zaccaria
Knolls Atomic Power Laboratory
Lockheed-Martin
Schenectady, NY 12301

Hakan Aksoy, Ronald M. C. So
Department of Mechanical and Aerospace Engineering
Arizona State University
Tempe, AZ 85287

Abstract

Laser Doppler Velocimetry (LDV) measurements were taken in a rectangular confinement into which issues a row of parallel jets. Two-component measurements were taken with two optics orientations yielding three mean velocity components and four Reynolds stress components. As observed in isolated three dimensional wall bounded jets, the transverse diffusion of the jets is quite large. The data indicates that this rapid mixing process is due to strong secondary flows, transport of large inlet intensities and Reynolds stress anisotropy effects. Navier-Stokes analyses of this configuration underpredict the rate of transverse jet diffusion. Detailed numerical accuracy studies show that this is attributed to shortcomings in low-Reynolds number two-equation turbulence modelling. A low-Reynolds number full-Reynolds stress model is shown to provide improvement.

Introduction

Three dimensional bounded jets are important in a variety of engineering applications including turbine blade, gas turbine combustor and microcircuit cooling, thrust vectoring nozzles, airfoil boundary layer control and ventilation system exhaust. Mixing of bounded jets with adjacent jets or with their surroundings (i.e. transverse and boundary normal momentum and heat transfer), plays a crucial role in the effectiveness of the injected flow in these applications. A considerable body of research has been performed which studies different classes of bounded jets. These include: jets bounded by free surfaces and solid walls, planar and three-dimensional wall jets, jets bounded by one plane wall, two parallel plane walls and axisymmetric walls (pipe and diffuser geometries), and systems with multiple interacting jets of various configurations.

The authors are interested in the mixing characteristics of parallel turbulent jets which issue into confinements bounded by two plane parallel walls. Navier-Stokes analyses performed on such configurations have yielded mixing rates (as quantified by the axial decay rate of the difference between maximum and minimum jet velocities) that are much smaller than the rapid decay rates observed in earlier, less detailed tests. Preliminary assessment of possible explanations for this underprediction included grid resolution/discretization accuracy, boundary condition specification, mean flow unsteadiness, and turbulence modelling shortcomings.

As demonstrated below, numerical accuracy concerns were eliminated from consideration through grid and convection term discretization parameterization. Also demonstrated below, in the particular configuration tested, and discussed here, no large scale unsteady modes (i.e. jet "flapping") were present. However, conventional (viz. low-Reynolds number two-equation) turbulence models still yielded badly underpredicted jet decay. These observations indicated that turbulence modelling likely plays an important role in the prediction of Parallel Confined Jet (hereafter PCJ) mixing.

A large body of experimental research has been performed on related flows, which suggests that some of the physical mechanisms present in PCJ mixing are important in rapid transverse mixing in other bounded jet flows. Specifically, isolated 3D wall bounded turbulent jets have been studied by numerous researchers. Measurements by Newman et al. [1972], and many others, on 3D isolated wall bounded jets have shown that transverse jet growth rates in these flows are substantially larger than the growth rates normal to the wall. Physical mechanisms to which this anisotropic jet growth have been attributed include increased turbulence transport (i.e. $\frac{\partial}{\partial y}\overline{u'v'} > \frac{\partial}{\partial z}\overline{u'w'}$, see coordinate convention in Figure 1), and secondary flows of the first and second kind (Launder and Rodi [1983]). Also, Davis and Winarto [1980] took velocity and Reynolds stress measurements in an isolated 3D wall bounded jet and observed larger effective momentum diffusion transverse to the jet than normal to the bounding wall.

An isolated 3D wall jet bounded on two sides by a confinement has been studied by Holdemann and Foss [1975]. Their mean flow measurements showed strong secondary motions (streamwise vorticity) and large jet spreading rates.

Several nondimensional geometric scales can be adopted to characterize PCJ flows. The ratio of inlet nozzle hydraulic diameter to confinement height and jet spacing D_H/h, D_H/L (see Figure 2) and the nozzle aspect ratio are relevant and serve to distinguish the geometries investigated by others. Configurations of interest to the authors and investigated here are characterized by closely confined ($D_H/h \cong 1$), closely coupled ($D_H/L \cong 1$) and low aspect ratio jets ($AR \cong 1$).

PCJ configurations have been studied by Krothapalli et al. [1981]. They found that the spreading rates of a multiple rectangular jet configuration was not significantly affected by the presence of a partial confinement. However, the configuration considered here differs significantly from that of Krothapalli and his coworkers in that the aspect ratio of their rectangular jets was $AR \cong 20$ (vs. $\cong 1$ for the present geometry) and the normalized distance between their jets was $D_H/L \cong 5$ (vs. $\cong 1$ for the present geometry). Accordingly, the presence of a confinement in their experiments has significantly less influence on parallel jet mixing than observed here.

The purpose of the present PCJ measurement program was to take mean flow and Reynolds stress data of sufficient detail for improved understanding of the physics in these flows, and for turbulence model development and verification. The purposes of this paper are to present and interpret the experimental measurements taken in the PCJ configuration. Also discussion of the Navier-Stokes and turbulence modelling approaches taken to date in modelling this flow field are presented.

Nomenclature

Symbols

A_{xs}	Cross sectional area of test section (= 7.74×10^{-3} m^2)
$A_{xs1/4}$	Area of 1/4 jet cross section
h	Confinement height (= 0.0195 m)
L	Distance between adjacent jet centerlines (= 0.0762 m)
N	Number of samples taken
Q	Volume flow rate through facility (= 6.31×10^{-3} m^3/s)
$Q_{1/4}$	Volume flow rate through 1/4 jet cross section
R_e	Reynolds number based on h and U_{bulk}
R_e^*	Reynolds number based on h and U_{cl}
U, V, W	Mean cartesian velocity components
U_{bulk}	Bulk velocity in confinement (= Q/A_{xs} = 0.815 m/s)
u', v', w'	Fluctuating cartesian velocity components
x, y, z	Cartesian coordinates as defined in Figure 1

Superscripts and Subscripts

*	Quantity directly measured via side scan
cl	Confinement centerline (z = 0.0 m)
jcl	Centerline of jet 3 (y = 0.2032 m, z = 0.0 m)
mcl	Midpoint between jets 2 & 3 (y = 0.1651 m, z = 0.0 m)
L1	Laufer (1950) 1" channel
L2	Laufer (1950) 5" channel

Experimental Configuration and Measurement Program

Figures 1 and 2 show sketches of the test section and optical configuration used for the measurement program. The coordinate convention utilized throughout is also presented in Figure 1. Five pipes of diameter D = 0.0381 m and 22 diameters long issue into a confinement. The confinement is 0.01905 m in height, 0.4064 m wide and 0.7620 m long. The axis of the third pipe is coincident with the centerline of the confinement. The pipe centerlines are spaced 0.0762 m apart. The end walls (y = 0.0 and 0.4064 m) were located 0.0508 m from the centerline of the outermost jets, rather than the 0.0381 m periodicity would suggest.

The dynamics of the parallel confined jet flow can be qualitatively characterized as follows. As the water flowing through each of the five inlet pipes nears the inlet to the confinement, it accelerates because the cross-sectional areas at the inlet to the confinement are smaller than the pipe cross sectional area (Figure 1). As the jets issue into the confinement, they decelerate due to a step increase in flow area, and begin to diffuse in the transverse (y) direction. Recirculation zones appear between each pair of jets due to this dump diffusion process. The jets mix out quite rapidly - the centerline axial velocity of jet 3 normalized by confinement bulk velocity decreases from 2.7 to 1.6 within approximately 5 confinement heights downstream of the inlet. As the jets mix out the region of the flow away from the endwalls develops towards a fully developed turbulent channel flow.

A 40hp variable speed centrifugal pump was used to control flow. The test section flow rate was measured to ± 1/2 % of reading using a turbine flow meter in the supply line to the test section. Flow rates through the five inlet pipes were controlled and measured to an accuracy of 2.5×10^{-5} m^3/s using rotometers in the individual pipe inlet lines. The volume flow rate of water through the facility was 6.31×10^{-3} m^3/s (100 gallons/minute). The flow split was controlled via valves downstream of the rotometers. This flow split was optimized through trial and error to yield near periodicity of the three middle jets as discussed below. Loop temperature was controlled using resistance heaters located on the pump suction piping and chilled water through a heat exchanger as necessary. The loop temperature was held constant at 38 °C. The corresponding Reynolds number of the inlet pipe flows based on pipe bulk velocity and diameter was 61000. Test section pressure was 1.5 psig, measured just upstream of one of the inlets to the test section.

The test section was designed using clear cast acrylic. To minimize distortion of the beams through

the test section walls, the cast acrylic was milled to a 0.13 mm tolerance on thickness and polished to retain optical clarity. A water box (not shown in figures) was fitted on top of the test section so as to allow submersion of the probe as discussed below.

A four-beam backscatter laser doppler fiber optic velocimetry system was used to take the velocity measurements. A 122 mm focal length lens was utilized with the probe, producing a measurement volume 0.32 mm long and 0.06 mm wide in water. The fiber optic probe was supported above the test section with a beam mounted to a milling machine which controlled traversing, with an estimated maximum positional error of ± 0.25 mm. Neutrally buoyant latex seed (5 μm) was used for the LDV measurements. Water added to the loop was deaerated to minimize the presence of bubbles in the flow stream. In all cases the beam powers were maintained between 30 and 60 mW for the green (514 mm wavelength) beams and between 10 and 20 mW for the blue (488 mm wavelength) beams. A 4W Argon laser generated the beams.

A digital burst correlator was used to process the LDV data. This processor discriminates signal from noise using auto-correlation instead of amplifying detection. A total of 256 digital samples per doppler burst were analyzed to calculate a single velocity measurement. A 40 MHz Bragg shift was applied to one beam of each of the beam pairs to enable measurement of zero and negative velocities. Coincidence between the two velocity components was achieved by requiring the two measurements be within a specified time interva. This interval was based on the minimum residence time of a seed particle in the measurement volume. For this experiment, the coincidence interval specified was 100 μs. The coincidence data rate varied between approximately 10 Hz and 300Hz, depending on the proximity of the measurement volume to the wall. 3000 samples were taken at each point to maximize statistical certainty. A transit time weighting scheme was used to correct the velocity data from biases due to turbulent fluctuations (Barnett and Bentley [1974]).

Two sets of scans were performed. Referring to Figure 2, these are designated as "top" scan ($\theta = 0$) and "side" scan ($\theta = 22^{\circ}$). For the side scans, the probe was submerged in a water box (containing de-ionized water) so that the beam bisector angles were the same between the lens and plexiglas top of the test section and within the test section. The end of the probe was fitted with a glass cover and sealed to be leak tight. This cover ensures a planar interface with the water and minimizes beam distortion which would cause changes in fringe spacing and ovalization of the beams; both produce significant errors. The choice of 22° for the side scan orientation was settled upon as follows. It is desirable to have beam bisectors be as nearly orthogonal as possible, for accuracy reasons, as discussed below. Coincident measurements were obtained with reasonably good data rates without beam steering, by using beam bisectors inclined as much as 22° to vertical. The top scans provide direct measurement of $\overline{U}, \overline{V}, \overline{u'u'}, \overline{v'v'}, \overline{u'v'}$ (see coordinate conventions in Figure 1). The side scans also provide direct measurement of $\overline{U}, \overline{u'u'}$, thereby providing some measure of repeatability. More importantly, the side scans provide the wall normal mean velocity, $\overline{W}$, and one other component of the Reynolds stress tensor, $\overline{u'w'}$, obtained through trigonometric manipulation. Specifically, referring to Figure 2:

$$\overline{W} = \frac{V^*}{\sin\theta} - \frac{V}{\tan\theta}, \quad \overline{u'w'} = \frac{\overline{u'v'^*}}{\sin\theta} - \frac{\overline{u'v'}}{\tan\theta} \qquad (1)$$

where unstarred and starred quantities are directly measured by top and side scans respectively.

As indicated above, considerable effort was put to generating a nearly periodic jet field in the central part of the test section. Pre-design Navier-Stokes analyses indicated that using five jets would provide reasonable periodicity in the three central jets.

The near periodicity of the jet field, reduced the total amount of data to be obtained, since three planes of symmetry could be exploited, as indicated in Figures 1 and 2. Additionally, analysis of the flow is simplified by reducing the required computational domain size. Near periodicity in the central three jets, and the x-y and x-z symmetries afforded by the geometry were realized, as verified by measurements presented below. Accordingly, relatively high resolution data was taken in a 1/4 jet section at twelve axial locations shown in Figure 2. Top scans were taken at all twelve stations. Side scans were taken at the six stations designated in the figure (Test section geometry and beam configuration precluded side scan traverses closer to the confinement inlet than x = 0.027 m). Figure 3 shows a typical cross sectional measurement scan grid. For the first 9 axial scan locations ($x \leq 0.1016$ m), a 13 x 8 traverse grid was used as shown in Figure 3. Superposed in this figure are contours of measured axial velocity at x = 0.0279 m downstream of the confinement inlet. As the jets mixed more thoroughly, well downstream of the inlet ($x \geq 0.1524$ m), a coarser traverse grid of 10 x 5 was utilized.

Experimental Results and Interpretation

Experimental Errors

LDV measurements are subject to numerous errors, most of which can be quantified. The total uncertainty can be found by combining precision and bias errors as: $U_{total} = \pm (B+tP)$, where B is the bias error, P is the precision error and t = 1.96 for a 95% confidence level (for a sample size greater than 50). Patrick [1987] states the bias errors include errors from laser beam geometry, signal processor errors and seeding bias errors. Most of the bias errors are very small

compared to precision errors (discussed below) and are thus neglected. The bias errors which can be of the same order of magnitude as the precision errors are velocity and angle bias. As mentioned above, the velocity bias error is corrected using transit time weighting, while frequency shifting was used to minimized angle bias. Thus the bias errors can be neglected.

The precision errors in LDV measurement are data processing errors which result from averaging a finite number of data samples per data point. In LDV measurements the velocity being measured does not remain constant during the sampling period, but fluctuates due to turbulence. Thus the precision error in the mean velocity, assuming a normal distribution of velocity samples, is:

$$\frac{S_{\overline{V}}}{\overline{V}} = \frac{1}{\sqrt{N}}\left(\frac{V'}{\overline{V}}\right), \qquad (2)$$

where $\overline{V}$ is the sample mean velocity, and $V'/\overline{V}$ is the local intensity. Patterson [1982] states that the mean square turbulence intensity has a Chi-square distribution. For a large sample size (N>50) the precision error of the turbulence intensity measurement can be found from:

$$\frac{S_{v'}}{v'} = \frac{1}{\sqrt{2N}}. \qquad (3)$$

For the LDV measurements taken here, 3000 axial and tangential coincident samples were taken at each measurement position. This gives an uncertainty of approximately ± 2 % inside the jet, ± 4 % in between the jets for both U and V and 1 % for $\overline{u'u'}$ and $\overline{v'v'}$ (these errors based on normalization with respect to U_{bulk}). Since W was obtained by combining LDV measurements with the probe at two different angles, at different times, its uncertainty is larger. The increase in error in W is due to the lack of both temporal and spatial coincidence between the two measurements, and to the increase in uncertainty (as $\theta \rightarrow 0$) associated with using equation 1 to indirectly obtain W. Based on the analyses of Orloff and Snyder [1981], and Morrison et al. [1991] the uncertainty in W is estimated to be $\pm 8\%$ inside the jets and $\pm$ 16 % in the region between the jets. The Reynolds stress, $\overline{u'w'}$, was also calculated from the experimental data, its uncertainty is estimated to be ± 50 %.

Flow Field Characterization

Several initial characterization studies of the flow field were performed to verify the absence of large scale unsteady motions, to verify the desired symmetry and periodicity characteristics of the five jet flow and to characterize the flows well upstream and downstream of the confinement inlet.

Figure 4a shows an energy spectrum of axial velocity measured at the center of jet 3, 2 2/3 confinement heights downstream of the confinement inlet (x = 0.0508 m, y = 0.0 m, z = 0.0 m). The plot shows an FFT of the 500,000 data points taken at a average random acquisition rate of approximately 525 Hz. For the geometric length and mean velocity scales of the present configuration a turbulence scale range of approximately 100 Hz to 10000 Hz is anticipated. Clearly the spectrum only captures the larger scales of turbulence (the energy content of the smaller scales being aliased to lower frequencies). It exhibits no indication (peak) associated with long time scale quasi-unsteadiness associated with the "mean" flow (as may be manifested in jet "flapping").

Several transverse scans ($\overline{U}$ vs. y) were taken along the centerline of the confinement (z = 0.0 m). These served to provide guidance in adjusting the flow rate through the outer jets to maximize the periodicity of the center three jets. Figure 4b shows the data from the x = 0.0508 m scan, and illustrates the near periodicity achieved. The flow rate splits through jets 1 - 5, were 19.7, 20.2, 20.2, 20.2 and 19.7 % respectively of the total test section flow rate of 6.31×10^{-3} m^3/s (100 gpm). The axial momentum defect which appears at the centerline of each jet in this plot will be discussed below.

Figure 4c shows the nearly symmetrical scans of $\overline{U}$ vs. z along the centerline of jet 3 (y = 0.2032 m) at x = 0.0508 and x = 0.1016 m. Figures 4b and 4c serve to justify the use of the three symmetry planes exploited in a more detailed measurement program and in Navier-Stokes analysis, results of which follow below.

As the jets mix, the confinement flow approaches that of a fully developed 2D turbulent channel flow ($V, W \cong 0, U = U(z)$), in so far as 3D effects can be neglected (aspect ratio of confinement = 21.3). A detailed scan was performed in the z direction near the confinement outlet, 34.67 confinement heights downstream of the inlet station (x = 0.6604 m, y = 0.2032 m). Figures 5a and b show the measured axial velocity profile vs. z at this location. (Measured transverse velocity was no more than $0.007 * \overline{U}_{cl}$). The open symbols in Figures 5a-c correspond to data obtained very close to the confinement wall (z-zwall = 0.12, 0.19 mm). The measurement volume length of 0.32 mm in water indicates that the probe volume partially intersects the wall for these measurements. Though the measured values of mean velocity appear reasonable, the normal stresses appear to be unrealistically high (especially $\overline{v'v'}$). Accordingly, the uncertainty associated with these two points was deemed significantly higher than the uncertainty estimated below for all the other top scan data. A normalized wall shear stress of $C_f \equiv \tau_w / (\frac{1}{2}\rho U_{cl}^2) = 0.0065$ collapses the axial velocity reasonably well to a logarithmic law-of-the-wall profile as seen in Figure 5a. (A spline fit through

the first two data points yielded $C_f = 0.0057$). Laufer (1950) investigated several nearly fully developed channel flows including two of very similar Reynolds number to the PCJ configuration ($R_e^* = 24400, 24600$ vs. 23400 for PCJ). Laufer reported wall stress values of $C_f = 0.0036$ and 0.0038 for these two channels, significantly lower than the values deduced for the PCJ configuration. Consideration of this difference and of the mean velocity and turbulence intensity data in Figures 5b and c suggest that the Reynolds normal and shear stresses in the PCJ channel flow are significantly higher than in Laufer's channels. Results to follow indicate that the turbulence levels in the PCJ configuration are still decaying from their very large near-inlet values at this near-outlet location.

Figure 6 shows a plot of measured axial mean velocity in the inlet pipe to jet 3, 1.75 pipe diameters upstream of the confinement inlet ($x = -0.0667$ m). The profile is seen to be very close to axisymmetric, and compares well with a 1/7 power law distribution. Some evidence of the approaching confinement area step change is discernible in slight symmetric inflections near $z = \pm 0.01$ m ($z/h \cong \pm 0.5$).

Detailed Scans

Figures 7 and 8 present axial and transverse mean velocity data at the first 10 axial top scan locations. Figures 7a-j show front view contour plots of U and V, figure 7k shows a carpet plot of the $x = 0.0635$ m scan. Clearly, the data are quite smooth, and both mean velocity components were found to be repeatable to within 0.02 m/s. Figure 8 shows a top view of these data. Specifically, velocity vectors are superposed on contours of axial velocity at scan locations closest to the wall ($z/(h/2) = 0.859$) and at the confinement centerline ($z/(h/2) = 0.0$).

Several important features of the mean flow are obtained from the data in Figures 7 and 8:

Flow issuing into the confinement from the inlet pipe encounters a variable height "forward step", the maximum height of which occurs at the pipe/jet centerline. This gives rise to a large axial momentum defect at the jet centerlines. This defect is observed only very near the confinement wall at $x = 0.00508$. The size of this defect region grows in z and y over the first several scan locations. This is due in part to turbulence diffusion. Secondary flows which develop near the inlet (measurements presented below) likely also plays a role in this transport of low momentum fluid. The peak jet centerline velocity is seen to increase due to this blockage (see also Figure 10). The region of diminished axial velocity reaches the confinement centerline at $x = 0.027$ m. This may be considered the axial extent of the near potential flow core at the jet centerline. This centerline defect is observed all across the confinement from $x = 0.027$ m to $x \cong 0.15$ m where its influence is seen to wash out.

As the parallel jets issue into the confinement, a large recirculation appears between adjacent jets. This recirculation zone is seen to be significantly wider (Δy) and longer near the confinement wall than at the confinement centerline (Figures 7a-g, 8). Specifically, at the confinement centerline, $x_{reattach} \cong 0.063$ m, compared to $x_{reattach} \cong 0.069$ m at the scan location closest to the wall ($z/(h/2) = 0.859$). Figure 8 shows that the maximum magnitudes of reversed flow velocities are much larger near the confinement wall $|\vec{V}|_{max,recirc} \cong 0.67$ m/s vs. 0.51 m/s.

Downstream of the recirculation zone between jets ($x > 0.07$ m) significant negative V velocities were measured across the jet due to jet spreading (streamline divergence). Near the confinement inlet ($x = 0.0127$, 0.0216, 0.0270, 0.0381), however, relatively large transverse velocities near the wall are positive (towards jet centerline) and near the confinement centerline negative. The magnitudes of these transverse velocities reach nearly 0.4 m/s, compared to the cross-section bulk velocity of 0.82 m/s This suggests significant streamwise vorticity due to streamline divergence and secondary flows is also present in PCJ flow as discussed further below. Transverse velocities eventually diminish towards zero as the jets decay.

Figure 9 shows a plot of integrated volume flow rate vs. x. This serves primarily as a check on the velocity bias correction algorithm used, since near the inlet of the PCJ configuration, the turbulence levels and thereby velocity bias errors can be quite high. The measurements are seen to conserve mass well, considering the interpolation errors germaine to integrating the discrete cross-sectional data and the assumptions which must be made regarding the velocity distribution for the 14.1% of cross-sectional area between the confinement wall and the first scan location (a linear assumption was taken). The computed volume flow rate error is a maximum at $x = 0.0216$ m where $Q_{1/4}/Q_{1/4\ inlet} = 0.93$. Well downstream ($x > 0.1016$ m), a slight increase then decrease of the computed flow rate is observed, likely due to 3D effects associated with the endwalls (see Figure 4b).

In Figure 10, the axial jet decay along the confinement centerline is presented as a plot of normalized difference between measured axial velocity at the jet 3 centerline ($y_{jcl} = 0.2032$ m) and at the symmetry plane between jets 2 and 3 ($y_{mcl} = 0.1651$ m). Data from the 12 top scan and 6 side scan profiles are plotted. The difference between U_{jcl} and U_{mcl} increases near the inlet as discussed above, reaching a maximum of $(U_{jcl} - U_{mcl})/U_{jcl} \cong 1.25$ at $x = 0.027$ m. The jets then mix out quite rapidly, falling to $(U_{jcl} - U_{mcl})/U_{jcl} \cong 0.3$ at $x = 0.152$ m.

Also presented in Figure 10 is mass weighted average axial turbulence intensity, defined as:

$$\overline{T} = \frac{1}{U_{bulk}} \sqrt{\frac{\int_{A_{xs1/4}} \overline{uu} U dA_{xs1/4}}{\int_{A_{xs1/4}} U dA_{xs1/4}}} \qquad (4)$$

plotted vs. x. This intensity is seen to increase rapidly near the inlet, reaching approximately 0.45 at x = 0.0508 m. The turbulence intensity then decays exponentially. At x = 0.6604 m the average turbulence intensity is approximately 0.08, and still apparently decaying (see Figure 5c and discussion).

Figure 11 shows selected comparison of measured axial and transverse intensities at three axial locations. The three selected scans are located: a) very near the confinement inlet (x = 0.0051 m), b) approximately halfway along the axial extent of the recirculation zones (x = 0.027 m) and c) approximately two confinement heights downstream of reattachment (x = 0.1016 m). Very near the confinement inlet, turbulence intensities are quite small except near the wall and at the interface between the incoming jet and the recirculation region between jets, where maximum local intensities, $\sqrt{\overline{u'u'}}/U_{local}$, of approximately 25 % are observed. At x = 0.027 m intensities grow quite large in the vicinity of the jet-recirculation zone interface. The location of peak intensity shifts towards the jet centerline as the confinement wall is approached, consistent with the cross-sectional shape of the inlet (Figure 1). Turbulence levels at the confinement centerline remain small near the jet centerline since flow at this location has primarily been subject to relatively small normal strains. Transverse intensities exhibit the same trends as axial intensities at these first two scan locations, though the magnitudes of $\overline{u'u'}$ are nominally 50 % higher. Downstream of reattachment, $\overline{u'u'}$ and $\overline{v'v'}$ exhibit significantly different character. Specifically, in the defect region between the jets $\overline{v'v'}$ is larger than $\overline{u'u'}$, and diminishes monotonically toward the jet centerline. $\overline{u'u'}$ retains its upstream character of maximum magnitude near the location of maximum transverse shear ($\partial U/\partial y$).

The Reynolds shear stress data, measured via top scans, $\overline{u'v'}$, are plotted in Figure 12 at the same three representative axial locations. Qualitatively, these shear stresses follow gradient diffusion trends, as comparison with Figure 7 affirms. At x = 0.1016 m, effective transverse diffusion, $\nu_{t12} = -\overline{u'v'}/(\partial U/\partial y)$, is seen to steadily increase as the wall is approached (compare axial velocity and shear stress profiles at x = 0.1016 - refer to Figure 7k).

Figures 7-12 include only top scan data and axial velocity side scan data. As indicated previously, the primary motivation for the side scan measurements was to obtain W and $\overline{u'w'}$. Figure 13 shows measured cross flow velocity vectors at three axial stations where side scan data was taken (x = 0.0270, 0.0508, 0.0762 m). These vectors are formed from the resultant of V, measured directly from the top scans, and W, obtained indirectly from V and V* using equation 1. Qualitative comparison is made with finest grid Navier-Stokes solution discussed further below. At x = 0.0270 m clear evidence of two distinct secondary flow patterns is observed in the measurements. Specifically local crossflow velocity magnitudes reaching 25 % of local axial velocity are observed. These two secondary motions are characterized by crossflow toward the jet centerline near the confinement wall and away from the jet centerline near the confinement centerline. Note that for the entire jet, these motions correspond to Streamline divergence near the jet centerline and net crossflow toward the jet centerline in the recirculation zone are accessible from the data at this axial location. At x = 0.0508 m, only the secondary motion nearer to the jet centerline is still observable from this front view projection of the data. This scan is located near the end of the recirculation zone and therefore unlike the data in Figure 13c, shows net crossflow away from the jet centerline in the recirculation zone. Crossflow at x = 0.0762 m (Figure 13e) shows the same characteristics as at x = 0.0508 m, except that cross flow magnitudes are significantly diminished, as expected, since the jets are already fairly well mixed at this location. The magnitudes of the measured and computed secondary flows suggest that these motions play an role in transverse mixing including the development and persistence of the defect at the jet centerline (self-induction). Quinn [1994] found that such strong secondary motions played importantly in the off-center axial velocity peaks measured in high aspect ratio rectangular free jet.

The larger errors incurred in the non-coincident, indirectly obtained wall normal mean velocity measurements are clearly observable in Figure 13. Specifically, significant scatter in the measured W components are seen. As discussed above, error magnitudes for this quantity were estimated to be close to 0.1 m/s, compared to their nominal measured magnitudes of 0.2 m/s. Accordingly, erroneous scatter is observed at several locations, and these results should be judged as qualitative only. Also observable in Figure 13 are probable errors in measured V velocity. Specifically, positioning errors, inexact symmetry/periodicity of the flow and measurement uncertainty combine to yield unexpected values of V at certain locations (i.e. measured V $\neq$ 0 at jet centerline and the symmetry plane between jets). These errors are also evident in Figures 7 and 8.

Unfortunately, the measured Reynolds shear stresses, $\overline{u'w'}$, obtained indirectly from $\overline{u'v'}$ and $\overline{u'v'^*}$ using equation 1, were fraught with such large errors that even qualitative trends were difficult to extract. As discussed above, the combined uncertainties associated with positioning, non-coincidence, and

oblique access (indirect measurement) are significantly larger for Reynolds stresses than mean velocities. Accordingly, it appears that these errors rendered the accessibility of meaningful $\overline{u'w'}$ measurements unattainable in the present program.

Numerical Investigations

As suggested in the introduction, it was the authors' inability to accurately model the physics of PCJ configurations which precipitated the measurement program. More specifically, when CFD methods were applied to related configurations, and results compared to measured jet centerline axial velocity decay, analysis was seen to badly underpredict the decay rates. In this section, selected 3D CFD results of simulations of the present PCJ configuration are presented. These results serve to isolate turbulence modelling and transport (as opposed to numerical) issues as the primary factors in the poor prediction of PCJ mixing. Also, the (in)accuracy of conventional low-Reynolds number two-equation turbulence modelling approaches in these flows is quantified, and preliminary results obtained using low-Reynolds number full-Reynolds stress closure which show improvement are also presented. Lastly, the analytical results are shown to provide some physical insight into the measured flow field.

Several parameters were varied in order to assess numerical discretization requirements for these flows. Specifically, three flow solvers, a sequence of grids and various convection term discretizations were applied. For brevity, only those results obtained using two pressure based finite volume codes are presented, since all conclusions presented below can be drawn from the results of these analyses. One is a Full Navier-Stokes (FNS) colocated grid code and the other a Parabolized Navier-Stokes (PNS) staggered grid code. The FNS flow solver used, designated CFDS-FLOW3D, is commercially available. Features of this code, relevant to the present analyses include a multi-block capability, available second order accuracy (including boundary conditions and convection term treatment) and the authors' installation of the various turbulence models tested. The PNS flow solver, is a modified version of the TEACH code. This code uses 1st order accurate convection numerics and has served as a numerical test bed for numerous turbulence models.

The FNS studies are considered first. A fully developed axisymmetric turbulent pipe flow solution was generated using the flow code and this was used to construct pipe inflow boundary conditions for axial velocity and turbulence quantities. This inlet profile is included for comparison in Figure 6 with the measured profile. The model inflow boundary condition was located at x = - 0.1015 m, whereas the measurements displayed in Figure 6 (which show some evidence of the approaching confinement) were taken at x = - 0.0667 m. Constant static pressure and extrapolated transport scalars were applied at the exit boundary. Symmetry planes were applied as illustrated in Figures 1 and 2. A second order accurate implementation of the QUICK (Leonard [1979]) scheme was used for convection terms in the momentum equations. Standard second order accurate upwinding was used for convection terms in the turbulence transport equations.

Earlier studies applied two low-Reynolds number two-equation models to the PCJ configuration. These included models due to Chien [1982] and Launder and Sharma [1974]. Both models yielded very similar predictions for the PCJ configuration, especially if taken in comparison with how poorly they both do in predicting jet mixing. As the Arizona State University group became involved, a two-equation low-Reynolds number model due to So et al. [1994] (hereafter SAYS model) was applied. This model held more promise in that its ability to predict planar wall jets has been demonstrated (Gerodimos et. al. [1995]) to be superior to numerous other two-equation models (including Chien and Launder-Sharma). Also the SAYS model exhibits much lower near wall grid resolution requirements than most other two-equation models, a fact that renders it a much more practical model for engineering applications. For these reasons, only two-equation results obtained using the SAYS model are included below.

Using the SAYS model and second order accurate convection numerics, a grid study was performed to quantify the inaccuracies incurred due to turbulence modelling. As justified above, the PCJ configuration was approximated as an infinite row of confined jets. This allows exploitation of three planes of symmetry as shown in Figures 1 and 2. Specifically, the computational domain consists of only 1/4 of jet 3. This allowed grid refinement studies to be performed in reasonable turnaround times. The computational domain extended from x = - 0.1015 m (into the inlet pipe) to x = 0.762 m, consistent with the length of the test section. Four block meshes were used for these computations (3 blocks for inlet pipe, 1 for confinement). A fine mesh of the 1/4 jet configuration which consisted of 97400 nodes is shown in Figure 14. This mesh was halved in each coordinate direction to yield a coarser mesh consisting of 12175 nodes.

In Figure 15, comparison is made between the axial jet decay results obtained using these two CFD models and the PCJ measurements. Clearly, both FNS simulations underpredict jet decay badly. Also included in Figure 15 are results obtained using the PNS code. In the PNS analysis a 61 x 61 cross stream mesh and 400 axial locations were used. Comparison between solutions obtained with a 61 x 61 mesh and those with a 41 x 41 mesh were nearly identically, and therefore the 61 x 61 mesh was deemed sufficient. Inlet boundary conditions were constructed from the PCJ measurements at the first axial location where no negative mean axial velocities were measured (x = 0.0762 m). The SAYS model and a near wall full-Reynolds stress model due to So et al. [1994] (hereafter NWRS) were implemented. As with the FNS results, the PNS results show

significantly underpredicted jet decay, when the SAYS model is used. This despite the inflow boundary location being 4 confinement heights downstream of the inlet. These FNS and PNS results serve to isolate shortcomings associated with low-Reynolds number two-equation turbulence modelling, as opposed to numerical accuracy issues, as the dominant source of jet mixing underprediction in PCJ analysis.

A number of possible reasons exist for the poor performance of low-Reynolds number two-equation models in this flow field. These include anisotropy in the effective diffusion tensor, turbulence transport effects (discussed below), the linear gradient diffusion assumption, known to be inaccurate in planar wall jets, poor predictive capabilities of these models in recirculating flows, and the empirical and isotropic near wall damping functions, which are tuned to damp diffusion in wall normal directions without regard to concomitant transverse damping.

The effects of turbulence transport were investigated by parameterizing inflow boundary conditions in the FNS simulations. Figure 16 shows a comparison of predicted vs. measured jet defect and axial turbulence intensity decay. In each of these plots, the three curves corresponding to analysis represent calculations using the pipe inflow boundary conditions constructed as detailed above (which closely match measured inflow pipe measurements - see Figure 6), and two other calculations where the inlet turbulence levels were doubled and tripled respectively. The goal here was to attempt to approach the large measured near-inlet values to see if the transport of such high levels plays a dominant role in the jet mixing. These results indicate that increasing inlet turbulence levels can play a role in enhancing jet mixing. However, even tripling the inlet value only reduces the error in normalized jet velocity decay predictions by about 15%. The measured peak intensity occurs significantly downstream of all predictions. This indicates that improved turbulence modelling of the very complex inlet region could yield transport induced mixing enhancement of significantly more than 15%.

In principle, full-Reynolds stress closures can provide improved predictions of mean flow and turbulence quantities compared to two-equation models in flows where effective diffusion anisotropy, strong anisotropy in Reynolds normal stresses and/or significant deviation from linear gradient diffusion assumptions are present. Accordingly, the foregoing results and discussion suggest that full-Reynolds stress closure may improve jet mixing predictions in PCJ configurations. In Figure 15, PNS computations are also included which utilized the NRWS model. Clearly, the axial jet mixing rate is predicted with significant improvement compared to the two-equation model.

In Figure 13, the qualitative similarity in secondary velocity predictions and measurements yields some insight into the nature of the near inlet flow. Specifically, predicted cross-flow velocity vectors (superposed on contours of axial vorticity) are presented for the three planes coincident with the side scan measurements, and also for two planes closer to the confinement inlet (x = 0.0064, 0.0127 m). Clearly the two secondary flows measured and computed arise due to mixing at the jet-recirculation zone interface very close to the inlet. These axial vorticities then separate from one another less than one confinement height downstream of the inlet, and continue to be convected and diffused as indicated in the measurements and predictions. As indicated above, such motions can play importantly in jet mixing processes, but the Navier-Stokes analyses presented strongly suggest that turbulnce effects dominate.

Conclusions

Detailed LDV measurements were taken in a parallel confined jet configuration. Two optics orientations yielded three components of mean velocity and four Reynolds stresses. A series of numerical studies of this flow were also performed. Several conclusions were drawn from the measurements and Navier-Stokes analyses:

Test section design and tuning the flow rates in the outermost inlet pipes gave rise to a nearly periodic flow for which three planes of symmetry could be exploited in the measurement program and Navier-Stokes analyses.

Top scans provided accurate and detailed resolution of the development of quantities obtained directly with these scans. These measurements and corroborative Navier-Stokes analyses provided insight into the complex mean flow and turbulence physics of this flow.

Submerging the end of the LDV probe in water enabled side-scan measurements without beam steering. Axial mean flow and intensity measurement repeatability was good when compared to top scan measurements. However, non-coincidence and the indirect method of obtaining W and $\overline{u'w'}$ (viz. through trigonometric identities) introduces significantly more uncertainty in these measurements than for quantities obtained directly in the top scan measurements. Accordingly, W data were deemed qualitative only, and $\overline{u'w'}$ data were not deemed accurate enough even for qualitative interpretation.

Mean flow measurements illustrate complex flow field characteristics including large recirculation zones between jets, strong secondary motions and peak axial velocities away from the jet centerline.

Turbulence intensities near the confinement inlet are quite high due to abrupt geometry change and dump diffusion there. Comparison of Navier-Stokes analysis with measurements indicates that transport of large inlet turbulence intensity plays a significant, but not dominant role in the rapid jet mixing observed.

Significant anisotropies in the axial and transverse intensities appear near the symmetry plane between jets. This persists well downstream. The Rey-

nolds shear stresses qualitatively follow gradient diffusion trends. However, effective transverse diffusion increases steadily as the wall is approached.

Detailed FNS and PNS studies were performed which demonstrate that shortcomings associated with low-Reynolds number two-equation modelling plays a significant role in the inability of CFD analysis to accurately model jet decay physics.

Implementation of a low-Reynolds number full-Reynolds stress closure has shown improvement over two-equation modelling.

Acknowledgments

The authors acknowledge the important contributions of Mike Armstrong, Ted Bagwell, Dave Edwards, Paul Harris, Ed Razz, Brett Siebert and Mike Weiner to this work.

References

Barnett, D., Bentey, H., 1974, "Statistical Biasing of Individual Realization Laser Velcoimeters," Proceedings of the Second International Workshop on Laser Velocimetry, Purdeu University, p. 428.

Chien, K., 1982, "Predictions of Channel and Boundary-Layer Flows with a Low-Reynolds-Number Turbulence Model," **AIAA Journal**, Vol. 20, No.1, p. 33.

Davis, M.R., Winarto, H., 1980, "Jet Diffusion From a Circular Nozzle Above a Solid Plane," **Journal of Fluid Mechanics**, Volume 101, Part 1, p. 201.

Gerodimos, G., So, R. M. C., 1995, to be published.

Holdeman, J.D., Foss, J.F., 1975, "The Initiation, Development, and Decay of the Secondary Flow in a Bounded Jet," **ASME Journal of Fluids Engineering**, September, p. 342.

Krothapalli, A. Baganoff, D., Karamcheti, K., 1981, "Partially Confined Multiple Jet Mixing," **AIAA Journal**, Vol. 19, No. 3., p. 324.

Laufer, J., 1950, "Investigation of Turbulent Flow in a Two-Dimensional Channel," NACA Report 1053, p. 1247.

Launder, B. E., Sharma, B. I., 1974, "The Numerical Computation of Turbulent Flows," **Computer Methods in Applied Mechanics and Engineering**, Vol. 3, p. 269.

Launder, B.E., Rodi, W., 1983, "The Turbulent Wall Jet - Measurements and Modelling," **Annual Review of Fluid Mechanics**, Vol. 15, p. 429.

Leonard, B. P., 1979, "A stable and Accurate Convective Modelling Procedure Based on Quadratic Upstream Interpolation," **Computer Methods in Applied Mechaincs and Engineering**, Vol. 3, p. 269.

Morrison, G.L., Johnson, M.C., Swan, D.H., Deotte, R.E., 1991, "Advantages of Orthogonal and Non-orthogonal Three-dimensional Anemometer Systems, **Flow Measurement Instrumentation**, Vol. 2, April, pp. 89-97.

Newman, B. G., Patel, R. P., Savage, S. B., Tjio, H. K., 1972, "Three-Dimensional Wall Jet Originating from a Circular Orifice," **Aeronautical Quarterly**, Vol. 23, p. 188.

Orloff, K.L., Snyder, P.K., 1981, "Laser Doppler Anenometry Measurements Using Non-orthogonal Velocity Components: Error Estimates," **Applied Optics**, Vol. 21., No. 2, pp. 339-344.

Quinn, W. R., 1994, "Development of a Large-Aspect-Ratio Rectangular Turbulent Free Jet," **AIAA Journal**, Vol. 32, No. 3, p. 547.

Patrick, R. W., 1987, "Flowfield Measurements in a Separated and Reattached Flat Plate Turbulent Boundary Layer," NASA CR-4052, March.

Patterson, R. W., 1982, "Turbofan Forced Mixer-Nozzle Internal Flowfield, I-Benchmark Experimental Study," NASA CR-3492, April.

So R. M. C., Aksoy H. , Sommer T. P. , Yuan S. P., 1994, "Development of a Near Wall Reynolds Stress Closure Based on the SSG Model ofr the Pressure Strain", NASA CR-4618.

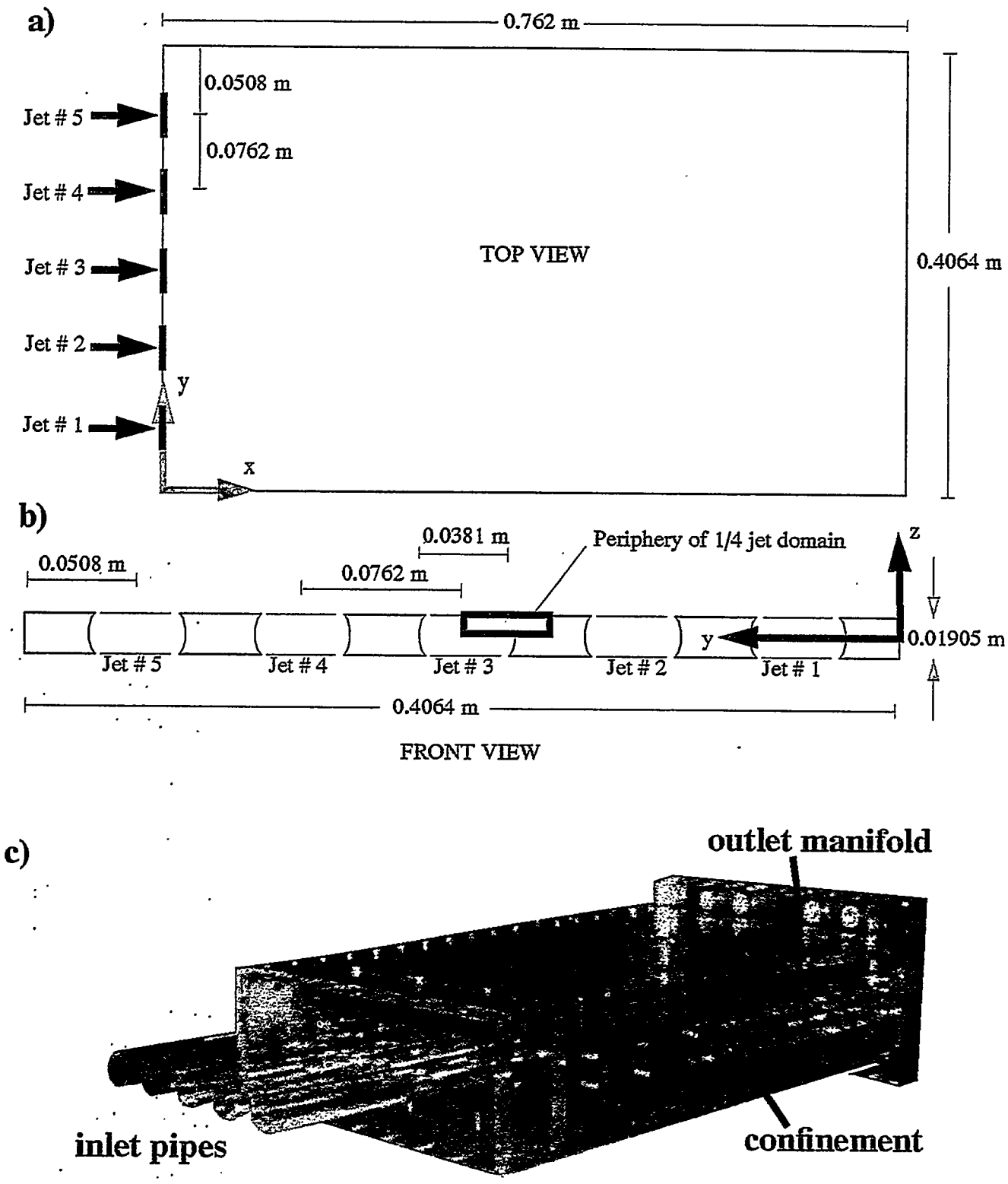

Figure 1. a) Top view, b) Front view sketches of Parallel Confined Jet test section. c) Photograph of test section prior to installation in laboratory.

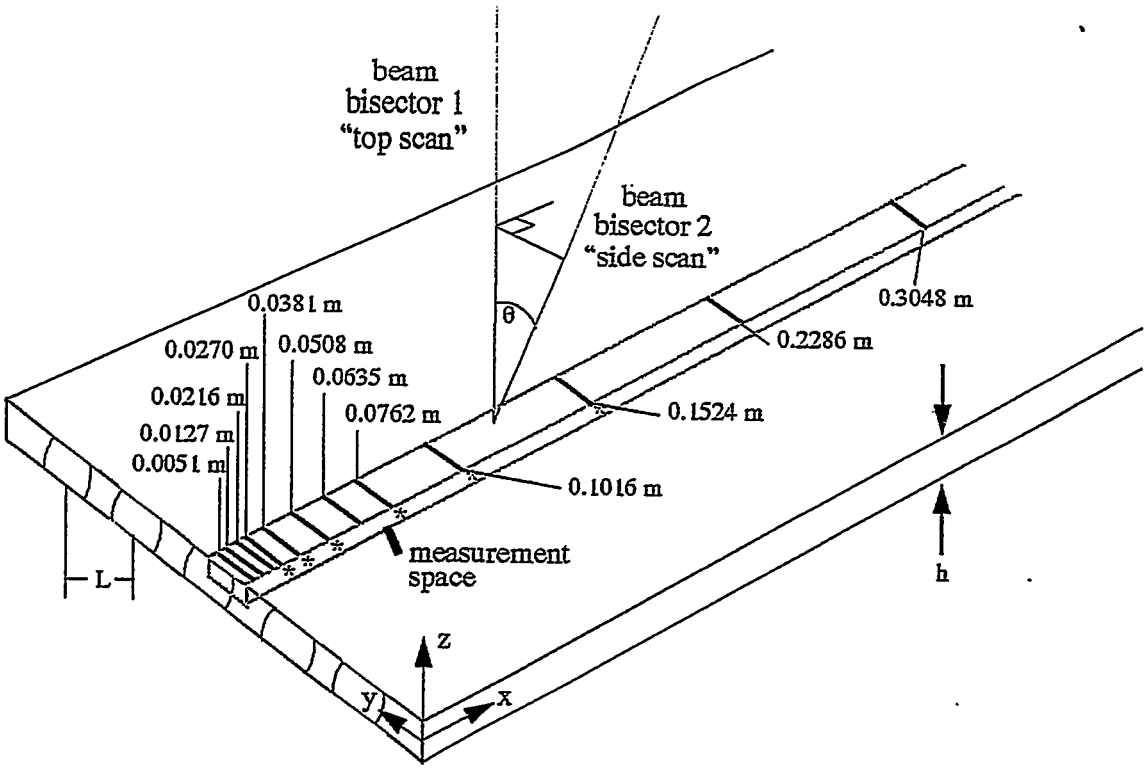

Figure 2. Sketch of two probe configuration and 12 top scan locations (not to scale). Side scans were also made at the 6 locations designated with a *.

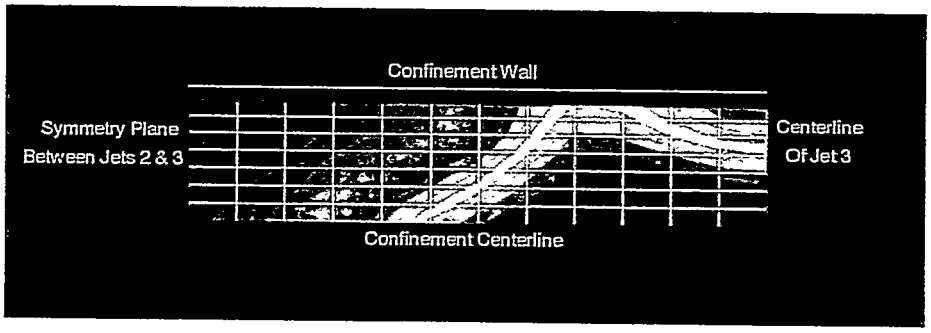

Figure 3. Contours of measured axial velocity 0.0279 m downstream of confinement inlet, illustrating the cross-stream resoution of scans in measurement space.

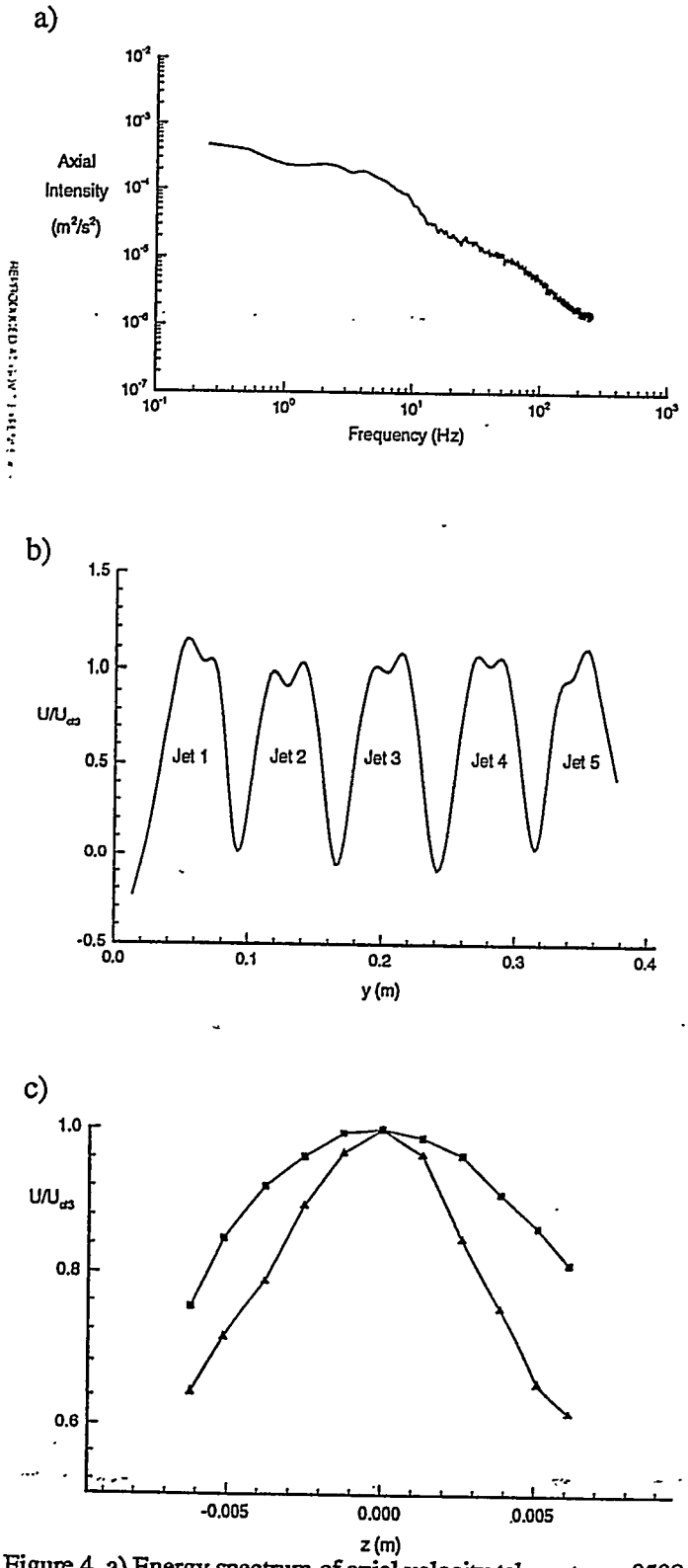

Figure 4. a) Energy spectrum of axial velocity taken at x = .0508 m , y = 0.0 m, z = 0.0 m. b) Measured axial mean velocity vs. y at x = 0.0508 m, z = 0.0 m. c) Measured axial mean velocity vs. z for jet 3 at y = 0.2032 m. for x = 0.0508 (▲) and 0.1016 m (■).

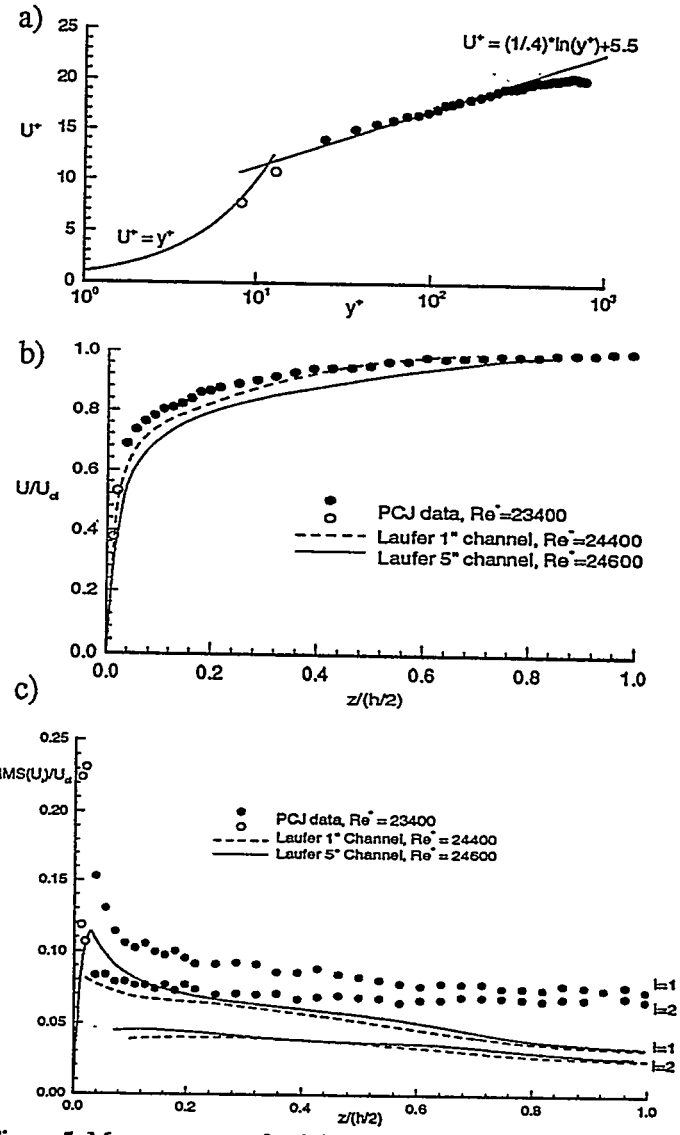

Figure 5. Measurements of axial velocity and normal stresses vs. z at x = 0.6604 m, y = 0.2032 m. a) Comparison of axial velocity with law-of-the-wall. b) Comparison of axial velocity with data due to Laufer [1950]. c) Comparison of normal stresses with data due to Laufer [1950].

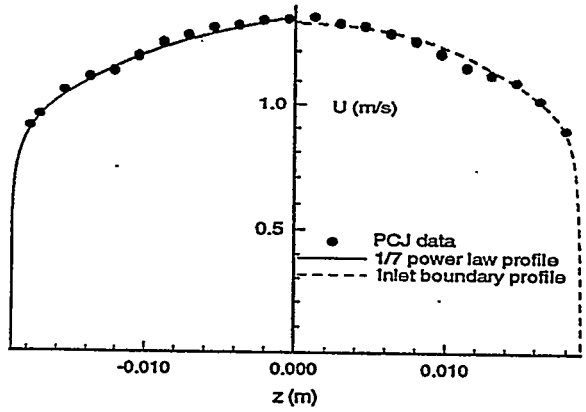

Figure 6. Comparison of measured axial mean velocity in the jet 3 inlet pipe at x = - 0.0667 m, with 1/7 power law profile.

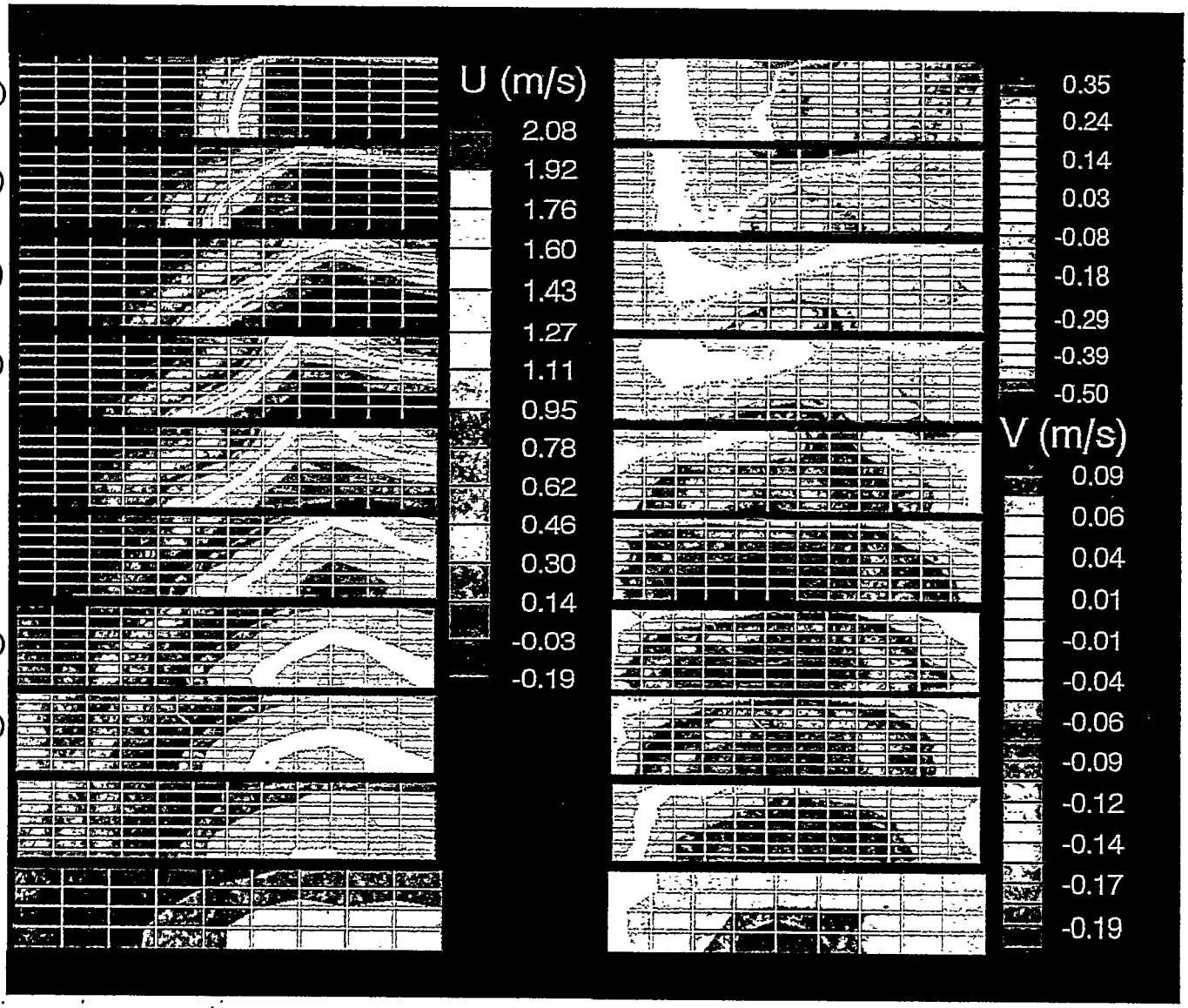

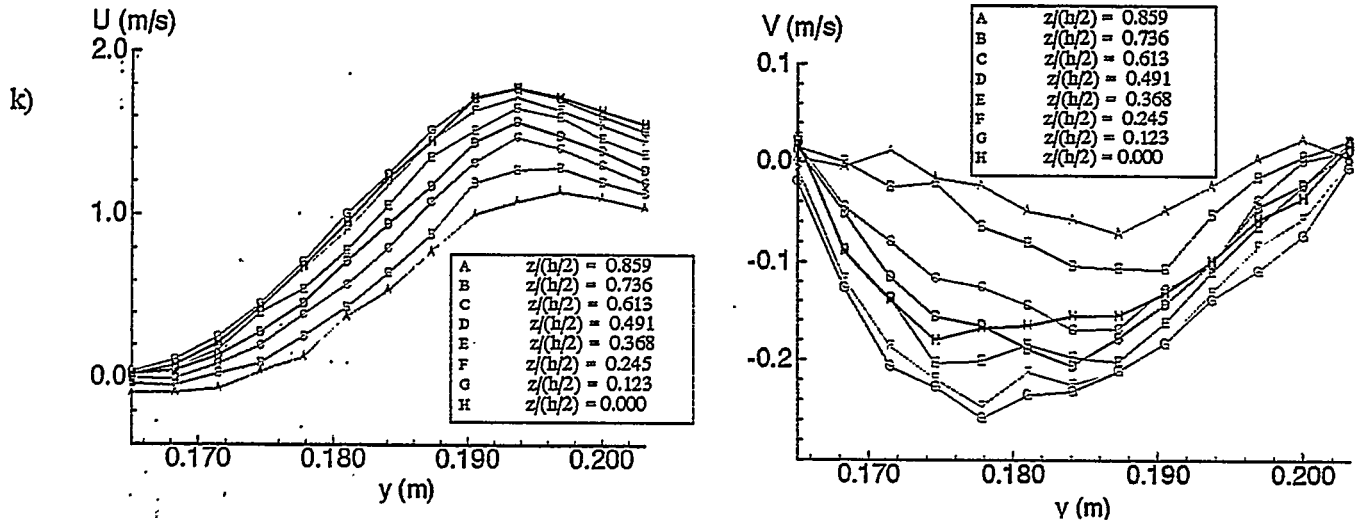

Figure 7. Measured mean velocities, U and V from top scan traverses. a) - j) are contour plots at x = 0.0051, 0.0127, 0.0216, 0.0270, 0.0381, 0.0508, 0.0635, 0.0762, 0.1016, 0.1524 m. respectively. Experimental scan location grid is overlaid on contour plots. Figure 3 shows relative position of confinement wall and symmetry planes for these plots. The "kink" in grid at x/h = 0.0762 is due to three modified y locations used to avoid a scratch in test section. k) shows sample carpet of these data at x = 0.0635 m.

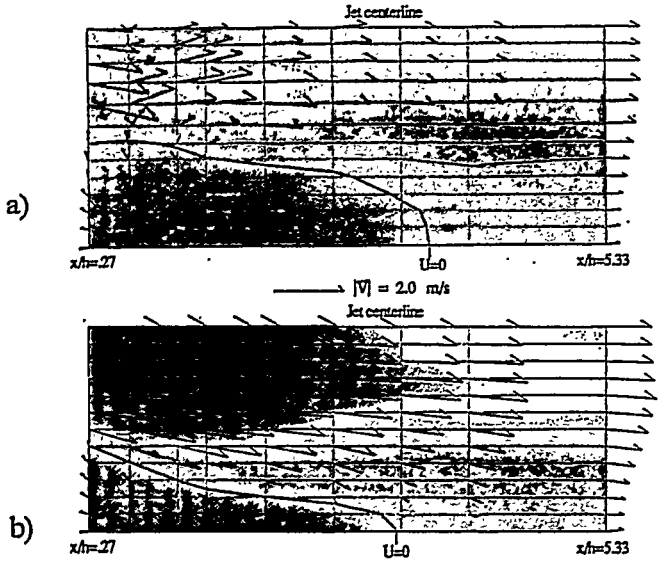

Figure 8. Top view of measured velocity vectors superposed on contours of axial velocity. a) scan plane adjacent to wall (z/(h/2) = 0.859, b) scan plane along confinement centerline (z/(h/2) = 0.0).

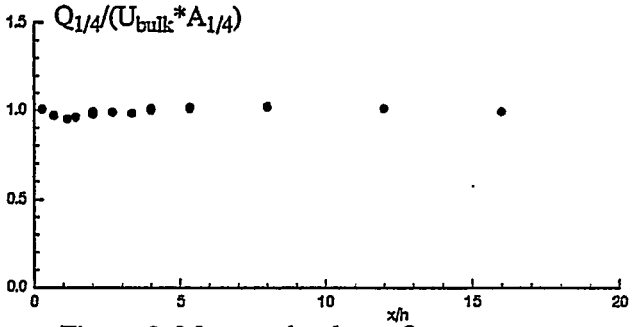

Figure 9. Measured volume flow rate vs. x.

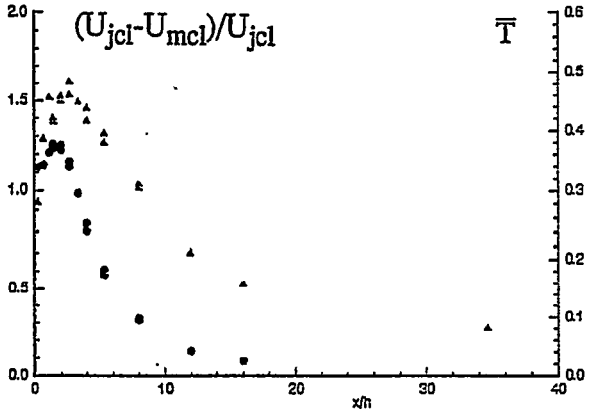

Figure 10. Measured axial distributions of jet 3 axial velocity decay (●) and mass weighted average axial turbulence intensity (▲)

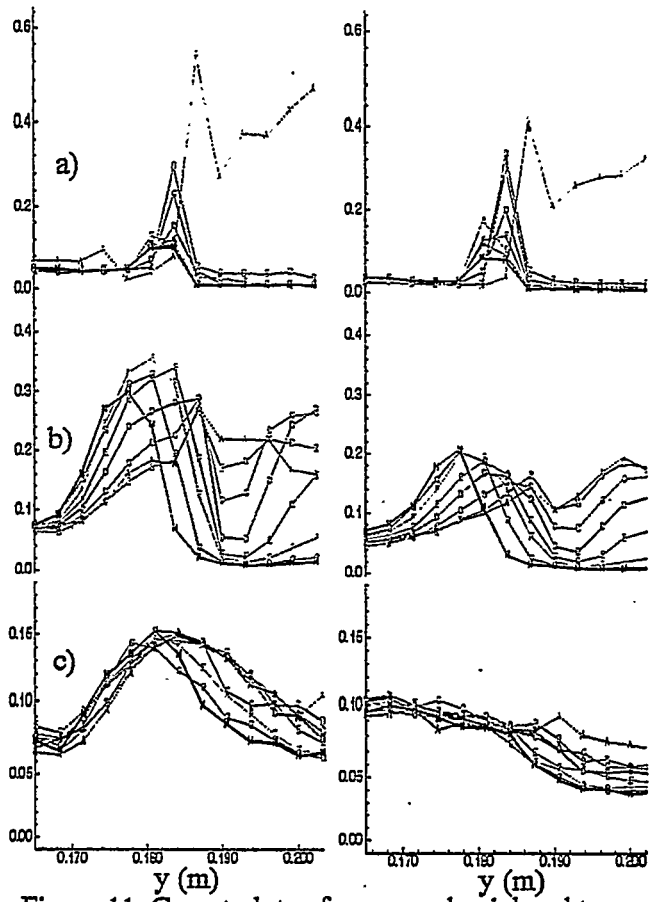

Figure 11. Carpet plots of measured axial and transverse intensities (m^2/s^2). Left column: $\overline{u'u'}$, right column: $\overline{v'v'}$. a) - c) at x = 0.0051, 0.027, 0.1016 m.

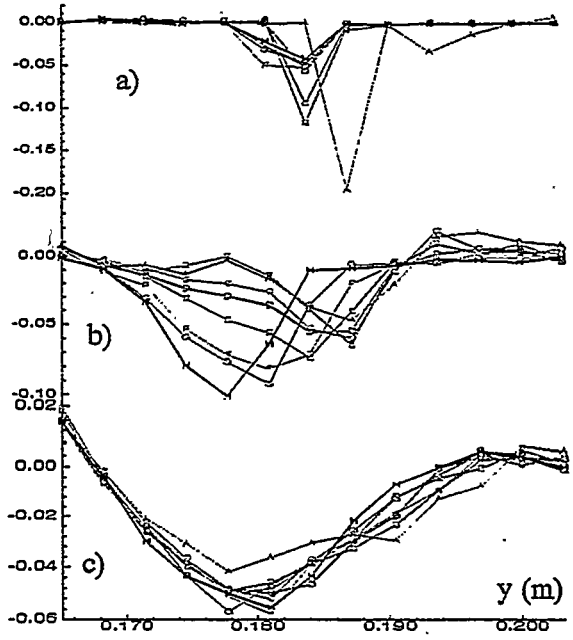

Figure 12 . Carpet plots of measured Reynolds stress, $\overline{u'v'}$ (m^2/s^2). a) - c) at x = 0.0051, 0.027, 0.1016 m.

Figure 13. Comparison of measured and computed cross flow velocities. a) - e) at x = 0.0064, 0.0127, 0.027, 0.0508, 0.0762 m.

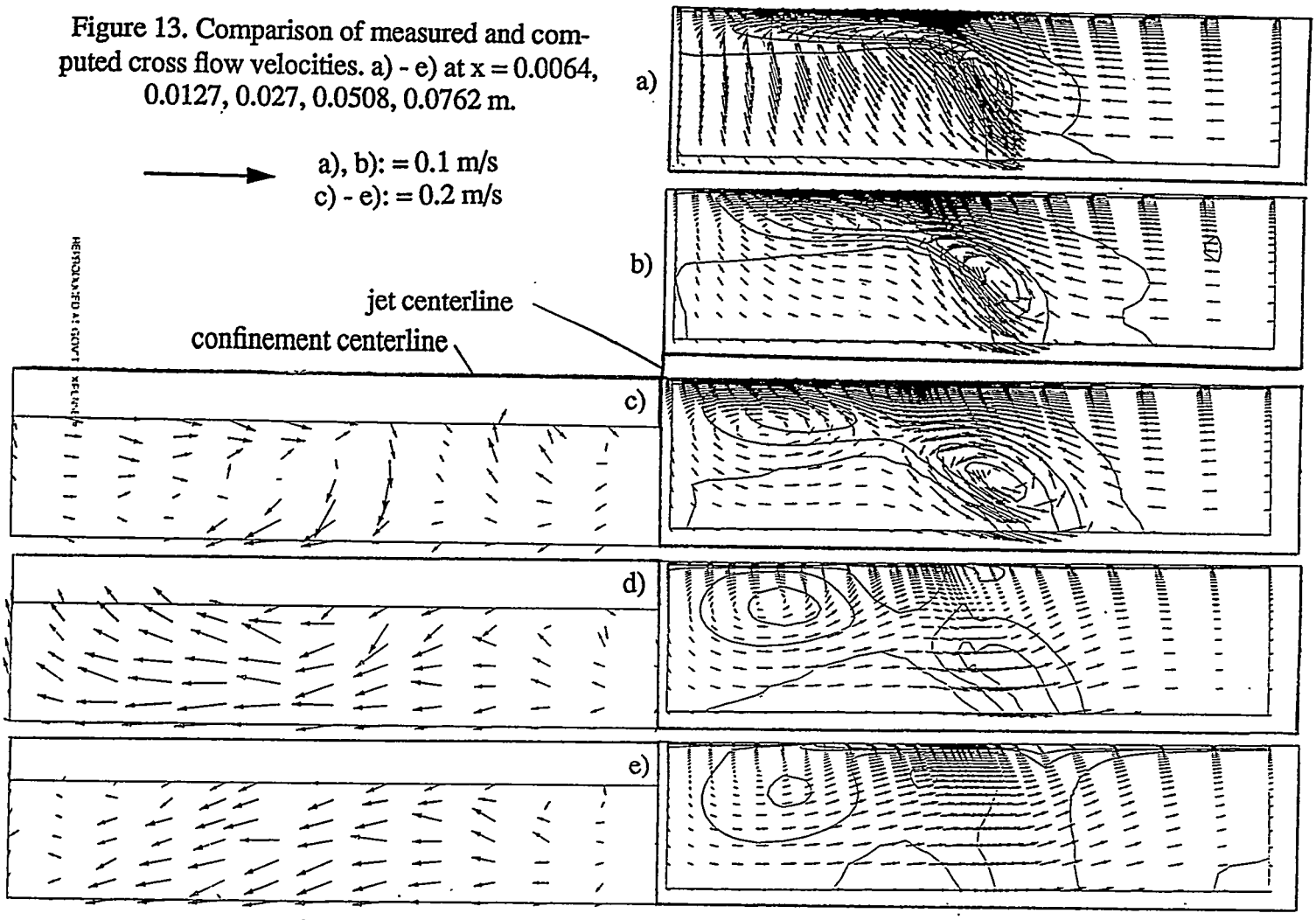

Figure 14. Selected planes of 97,400 node computational mesh used for 1/4 PCJ Navier-Stokes simulation.

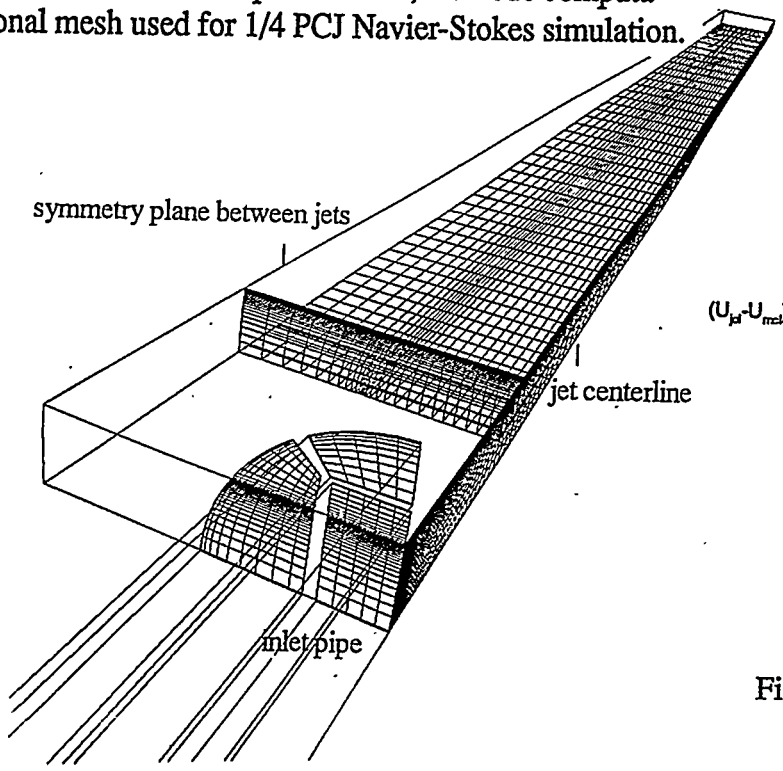

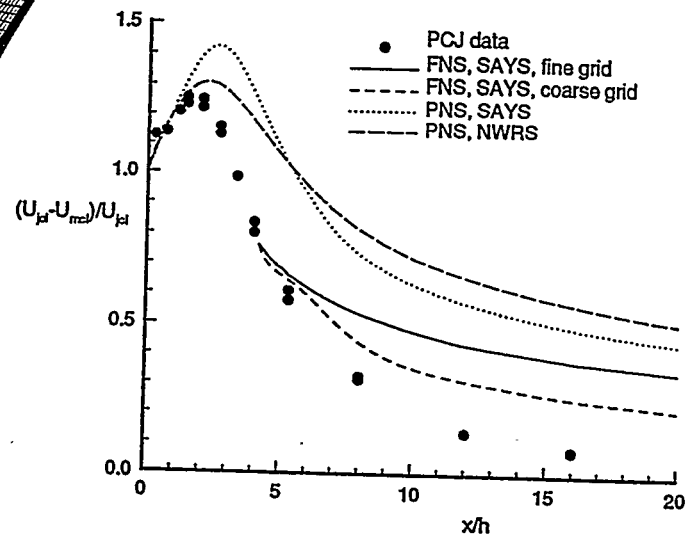

Figure 15. Comparison of measured and computed jet decay vs. x

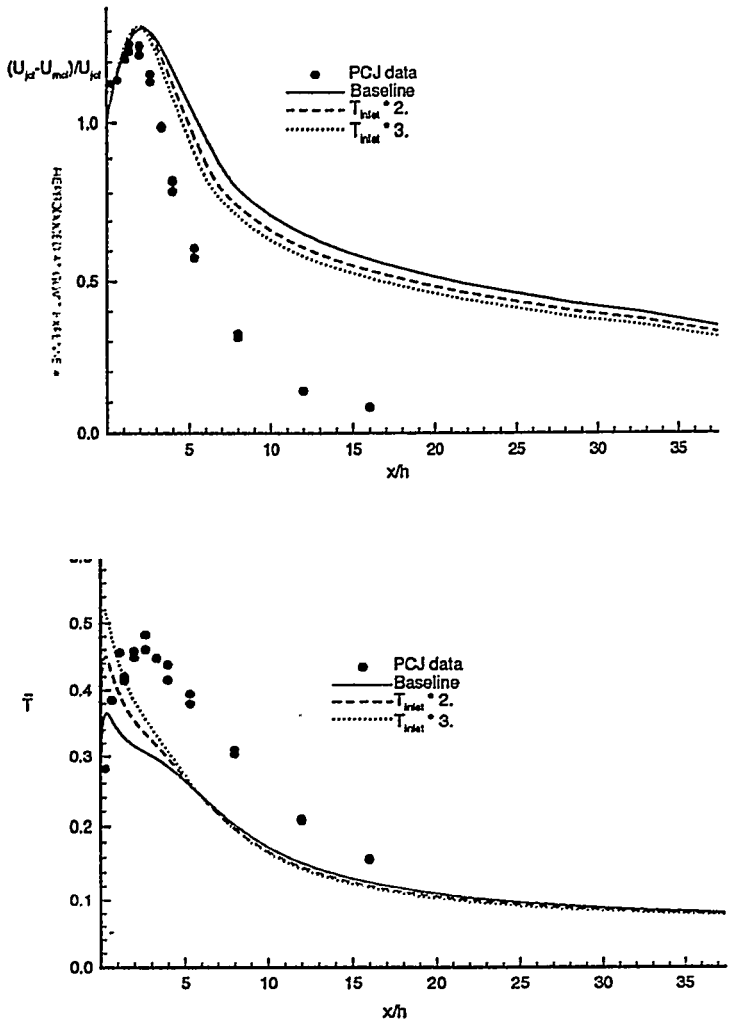

Figure 16. Comparison of predicted jet a) momentum and b) turbulence energy decay for three prescribed inlet turbulence intensities.

DISCLAIMER